Phys. Med. Biol., 1981, Vol. 26, No. 6, 965–983. Printed in Great Britain.

Computed tomography using proton energy loss

K M Hanson, J N Bradbury, T M Cannon, R L Hutson, D B Laubacher, R J Macek, M A Paciotti and C A Taylor†

Los Alamos Scientific Laboratory, PO Box 1663, Los Alamos, NM 87545, USA

Received 28 January 1981, in final form 15 May 1981

Abstract. An experiment has been performed to demonstrate the feasibility of proton computed tomography. The proton energy loss was used to measure the projections of the relative stopping power of the phantom. High quality reconstructions were obtained from scans of 19 cm and 30 cm diameter performance phantoms. Comparison with reconstructions from an EMI CT-5005 X-ray scanner showed the proton technique is more dose efficient by a large factor.

1. Introduction

The history of heavy charged particle radiography began in 1968 with the pioneering work of Koehler (1968). He showed that the addition of an aluminium foil 0.035 g cm^2 thick to a stack of aluminium absorbers, 18 g cm^{-2} thick, could be discerned by means of proton radiography using film as the detector. Subsequently, Steward and Koehler (1973a, b, 1974) and others (Cookson 1974, Moffett *et al* 1975, Kramer *et al* 1979) demonstrated that the high contrast images obtained by proton radiography provided improved imaging of low contrast lesions in human specimens over conventional X-ray techniques. The high contrast obtained in this energy-loss form of radiography is a consequence of the sharpness of the well known Bragg peak that occurs near the end of the proton range. Even higher contrast may be achieved through the use of heavy ions (Benton *et al* 1975, Capp *et al* 1978).

Although cited as a possibility by Cormack in 1963 (Cormack 1963, 1964), the first to apply charged particles to computed tomography (CT) was Goitein (1972). He employed projection data measured by Lyman with alpha particles to demonstrate the utility of his least-squares reconstruction algorithm. Later, in the comparison of heavy charged particle CT with X-ray CT (Crowe *et al* 1975, Huesman *et al* 1975, Cormack and Koehler 1976, Hanson 1978) it was shown that charged particles have a dose advantage over X-rays. This dose advantage might be utilised effectively by providing CT reconstructions with significantly better density resolution than is possible with X-rays at a given dose level. Furthermore, in charged particle CT, it is the linear stopping power relative to water that is imaged rather than the X-ray attenuation coefficient. The unique imaging characteristics of charged particles may prove to be beneficial in medical diagnosis.

In another form of charged particle radiography, nuclear scattering radiography, the particles that undergo large angle deflection by means of nuclear scattering are detected. The point of nuclear interaction is determined by tracing the measured

† Permanent address: Norfolk State College, Norfolk, VA, USA.

0031-9155/81/060965+19$01.50

directions of the particle, before and after the patient, to their intersection. This method, which has been successfully applied to the investigation of human subjects (Berger *et al* 1978, Duchazeaubeneix *et al* 1980), has entirely different imaging characteristics from the energy-loss methods described above.

In this article we present the results of an experiment designed to demonstrate the feasibility of obtaining high quality CT reconstructions from projections acquired through the measurement of proton energy-loss. The proton energy-loss method of obtaining the projections necessary for CT reconstructions is presented in section 2. Section 3 describes the apparatus used. The calibration and stability of the residual range determination are presented in section 4. The spatial limitations of the system and the method used to improve the spatial resolution are discussed in section 5. The proton CT reconstructions are compared with those produced by an X-ray scanner in section 6. In section 7 we present comparisons of dose efficiency and spatial resolution. Our conclusions are given in section 8. The peak fitting algorithm used in the data analysis is compared with improved methods in Appendix 1. The experimental results obtained with alternative residual range detection systems are presented in Appendix 2. Preliminary results of the experiment reported here have been presented elsewhere (Hanson 1978, Hanson *et al* 1978b, Hanson 1979a).

2. Method

The energy loss method of charged particle radiography is based upon the effect on the residual range of the particles caused by the material being radiographed. The energy loss incurred by protons of initial energy E_0 that follow a path of length L in some medium is given by

$$E_0 - E = -\int_0^L \mathrm{d}l' \, (\mathrm{d}E/\mathrm{d}x)(l') = \int_0^L \rho(l') S(l', E') \, \mathrm{d}l' \tag{1}$$

where E is the final proton energy, the integral is with respect to the position l' along the path, $(\mathrm{d}E/\mathrm{d}x)(l')$ is the linear stopping power of protons in the medium at l', $\rho(l')$ is the density of the medium at l' and $S(l', E')$ is the mass stopping power of the medium at l' evaluated at the proton energy E' there. Note that E' is implicitly dependent upon l' and is determined by evaluating equation (1) with l' as the upper limit instead of L. The range R_0 in a homogeneous medium for protons of energy E_0 is defined as the distance the protons travel before losing all of their energy

$$E_0 = \rho \int_0^{R_0} \mathrm{d}l' \, S(E'). \tag{2}$$

Consider the situation where protons of incident energy E_0 pass through a two-dimensional sample of possibly varying composition and density. Upon emerging from the sample, the protons' residual range ΔR is measured in some homogeneous reference material. The residual range may be shown from equation (1) to be given by

$$\Delta R = R_0 - \int \mathrm{d}l' \, \eta(x', y', E') \tag{3}$$

$$\eta(x', y', E') = \frac{\rho(x', y') S(x', y', E')}{\rho_{\mathrm{ref}} S_{\mathrm{ref}}(E')} \tag{4}$$

where R_0 is the range in the reference material corresponding to the incident energy E_0.

In this integral over the path followed by the protons through the sample, the cartesian coordinates x' and y' are specified by l'. The proton energy E' at l' is found using equation (1) as indicated above. In general, the contribution to the integral in equation (3) from any particular position (x', y') will depend upon the energy of the protons at that position which in turn will depend upon the path taken by the protons to reach that point. This implicit energy dependence means that ΔR is not simply related to the projection of a quantity that depends only on x' and y'. As such, ΔR does not yield projections that generally fit into the normal framework of CT reconstruction.

Proton mass stopping powers have the property that their ratios are approximately independent of proton energy. For example, using water as the reference medium, the difference in S/S_{ref} between 100 and 250 MeV is less than 0.01% for muscle (Janni 1966) and is only 0.2% for bone even though the linear stopping power changes by a factor of 1.87. For stainless steel, a metal sometimes found in patients, the difference is 2.1%. Thus, for a considerable range of materials η may be considered to be a function only of the material present at position (x', y') and the dependence upon proton energy may be neglected. Equation (3) then becomes

$$\Delta R = R_0 - \int \mathrm{d}l' \, \eta(x', y') \tag{5}$$

that is, the residual range is simply related to the projection of $\eta(x', y')$ along the proton path which is the required input for CT reconstruction. It is clear that the reconstructed quantity is $\eta(x', y')$, the ratio of the linear stopping power of the sample to that of the reference material. It will be noted that in non-biological applications if η is dependent upon proton energy for the materials being scanned, it may be necessary to correct the CT reconstruction in a manner similar to the beam hardening corrections employed for X-ray CT scans.

3. Apparatus

The experimental apparatus depicted in figure 1 was placed at the end of the P^3-West beam line at the Clinton P Anderson Meson Physics Facility (LAMPF). Viewing a target in the 800 MeV proton beam the P^3 channel was specially tuned to provide a nearly monoenergetic proton beam. The 240 MeV beam used to scan the 30 cm diameter phantom had a spot 1.6 mm (FWHM) wide by 3 mm (FWHM) high at its horizontal waist positioned at a depth of about 10 cm in the water bath. For the 19 cm diameter phantom, at 192 MeV, the spot was circular with a diameter of about 2.0 mm FWHM. The beam was restricted to a 0.4% energy bite in order not to affect the width of the detected residual energy distribution. The stability of the mean proton energy will be discussed in section 3. The horizontal beam divergence was about 14 milliradians (FWHM). Pion contamination in the 192 MeV proton beam was measured to be 0.4%.

Protons that traversed the water bath and phantom without significant deflection were detected in a position sensitive proportional chamber (PC), two scintillation counters (S1 and S2), and a hyperpure germanium detector (HPGe). The signals from S1 and S2 were taken in coincidence with the HPGe detector to form the master event trigger. The horizontal position of each proton was determined at a distance of 1.7 cm behind the water bath from time delay measurements of the signals detected at both ends of the cathode delay-line of the proportional chamber. S2 confined the events to protons that fell on the central region of the HPGe to eliminate edge effects. The active region of S2 was defined by a 2 cm diameter, 2.9 mm thick, plastic scintillator (NE102)

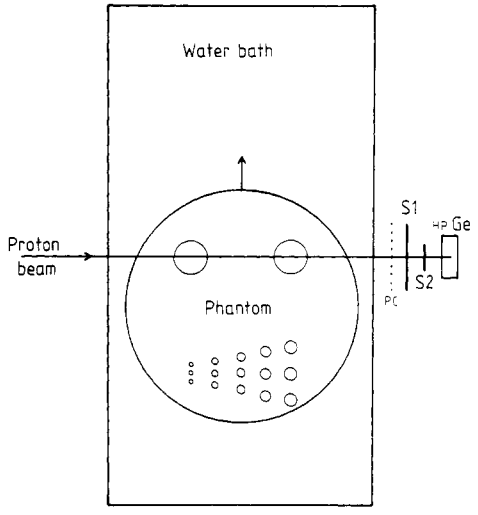

Figure 1. Schematic layout of apparatus. The proton beam as well as the detectors remain stationary. The CT scanning is accomplished by translation and rotation of the phantom.

disc, embedded in the centre of a Plexiglas light guide of like thickness to avoid energy disruption of protons that happened to traverse the edge of the scintillator. S2 was located 4.4 cm behind the water bath and 1 cm in front of the HPGe crystal. S1 was 3.0 mm thick.

The protons came to rest in the hyperpure germanium detector which measured their residual energy. The crystal had a diameter of 3.3 cm and a thickness of 1.25 cm, sufficient to stop a 70 MeV proton. The gain of the preamplifier was set to accommodate the detection of thousands of high energy particles within the 500 μs LAMPF macropulse. Consequently, the resolution measured for ^{60}Co gamma rays, 15 keV (FWHM), was significantly worse than the crystal's intrinsic capability. The HPGe detector was chosen on the basis of its extremely good gain stability. The 0.2% RMS long term gain stability required by this experiment is easily achieved by the HPGe detector.

The water bath had a 3.2 mm thick Plexiglas entrance window that could be moved to vary the water thickness. The exit window was 3.2 mm thick aluminium. In addition to the material already mentioned, a 0.73 g cm^{-2} polyethylene absorber was placed between PC and S1 for the 19 cm scan to bring the mean residual energy within the operating range of the HPGe. For the 30 cm scan, 0.14 g cm^{-2} was used.

During the course of a scan, the phantom position was controlled by computer, using analogue servomechanism units, one for horizontal translation and one for rotation about a vertical axis. During the scans data were taken for 0.9 s intervals followed by short 0.2 s translational movements of 1.0 mm for the 19 cm diameter phantom and 1.25 mm for the 30 cm diameter phantom. Data were taken over a full 360° rotation at 1.33° increments for the 19 cm diameter phantom and one degree increments for the 30 cm diameter phantom. Reproducibility of the phantom position was measured to be ±0.2 mm in translation and ±0.1 deg in rotation.

Data taking was accomplished by means of standard CAMAC modules readout by a PDP-11/45 computer. The PC delay-line signal was processed by a time-to-amplitude converter (Canberra 1443). The HPGe output was amplified and shaped by a Tennelec

TC-205 shaping amplifier with a 0.5 μs time constant. These pulse heights were digitised using two Nuclear Enterprises 9060 analogue-to-digital converters (ADC). The eightfold buffering provided by these ADCs allowed the data to be acquired at an average rate of 740 events per second at about 50% electronic deadtime in the LAMPF beam macropulse environment (0.5 ms on, 7.8 ms off). At this rate about 10% of the events were rejected by pile-up logic set to detect the occurrence of another HPGe pulse within 2 μs of the event. The PDP-11/45 transferred unprocessed event data as well as phantom position information to magnetic tape for later analysis. The computer also controlled the scanning motions as well as partially analysing the experimental data to assure to the experimenters that all was going well.

4. Calibration and stability

The HPGe detector response was calibrated in terms of the residual range in water by scanning a Teflon block with 5 mm wide steps of increasing thickness. The block was immersed in a 20.5 cm deep water bath. Each step was 0.638 g cm^{-2} thick corresponding to an increment of 0.224 g cm^{-2} water equivalent range (Janni 1966). The block was placed near the beam entrance, to obtain the best spatial resolution (see section 4). Figure 2 shows the HPGe response in terms of proton energy. The energy calibration was obtained from the pulse height produced by a high energy proton beam which passed through the HPGe detector. The energy deposited was determined from the stopping power of germanium (Janni 1966) and the known crystal thickness.

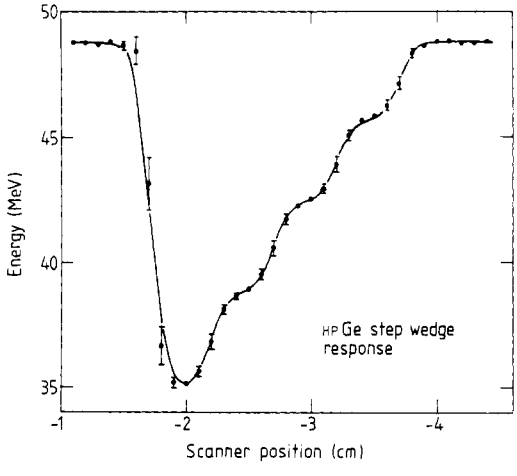

Figure 2. HPGe response to a Teflon step wedge. Fitting to data yields residual range calibration.

The data plotted in figure 2 were fitted by a function of the form

$$E = C(R_0 + \Delta R)^{\beta} \tag{6}$$

where ΔR is the alteration in the background range R_0 produced by the step-wedge for the reference material, water. The statistical uncertainty in the mean energy measured at each point was 0.04 MeV. In addition, an uncertainty in the position of 0.2 mm was assumed in order to reduce the influence of the spatial resolution function in the determination of the range–energy relationship. The width of the Gaussian resolution

function and the position of the step wedge were allowed to vary. The fitted values of $C = 34.93 \pm 0.06$, $R_0 = 1.895 \pm 0.001$ g cm^{-2}, and $\beta = 0{\cdot}522 \pm 0.025$ were obtained with $\chi^2 = 28.2$ for 29 degrees of freedom (E in MeV).

The dynamic range of the HPGe detector may be estimated from the knowledge that the range of the maximum energy of protons that can be stopped by the crystal is 4.0 g cm^{-2} in water. In order to extract the maximum amount of information from an ensemble of protons, the mean stopping position of the protons should be at least three standard deviations away from the front or back surfaces of the crystal. For an initial proton energy of 240 MeV, the range straggling is 0.40 g cm^{-2}. Thus, the effective dynamic range of the detector is 1.6 g cm^{-2} of water equivalent range. In order to stay within this limited operating range, a water bath was used and only low-contrast phantoms were scanned.

Any CT method requires the path length measurements to have long term stability in order to avoid artefacts or excessive low frequency noise in the reconstructions. The stability of the HPGe measurements of proton residual range was determined from a series of runs taken over a 35 min period. Each of these runs lasted 30 s and contained an average of 25,800 events. The data were obtained for an incident proton energy of 192 MeV with a 20.5 cm thick water bath. The mean peak energy was determined for each of the 39 stability runs using the optimum weighting function for the iterative moment technique (Appendix 1). The RMS deviation of the peak location was measured to be 26.4 ± 3.0 keV or expressed in terms of residual range, 1.96 ± 0.22 mg cm^{-2}. The expected uncertainty in the range determination determined from the shape of the energy spectrum and the mean RMS width of the individual fits is 27.4 keV or 2.04 mg cm^{-2} based on 25,800 events. Comparison of the measured RMS deviation with this expected value leads to the conclusion that the upper limit (90% confidence) on the RMS drift in the range determination over 35 min is 0.94 mg cm^{-2}. The residual range method used here was indeed very stable! Expressed differently, the upper limit on the RMS drift in the incident proton energy was 4.4 keV or 0.0023%.

5. Spatial resolution

In passing through matter all charged particles undergo numerous small-angle deflections caused by their interaction with the Coulomb field of the nuclei present. The resultant multiple Coulomb scattering produces a divergence in an initiall collimated particle beam that is unavoidable. Figure 3 shows the effect of multiple Coulomb scattering on a 230 MeV proton beam in its traversal of 30 cm of water. The FWHM envelope of the beam ultimately broadens to 14 mm at the rear of the water bath (Hanson 1978). The width of the proton beam is directly related to the spatial resolution in the CT reconstruction. A spatial resolution of 14 mm FWHM is intolerable for medical purposes.

Fortunately, the effective width of the proton beam can be reduced by constraining the protons to leave the water bath at a particular lateral position. The effect of this constraint is shown in figure 3. The proton beam is widest near the centre of the water bath where it has been reduced to a FWHM of 2.2 mm. Of course, the effect of the initial beam width, 1.6 mm FWHM in this experiment and beam divergence, 14 milliradians, as well as the width of the exit constraint must be folded into the beam profile. In this experiment, the exit position of each proton event was measured. The constraint on the exit position was placed on the events in the analysis. Thus, all the events could be used and no sacrifice in dose efficiency was incurred.

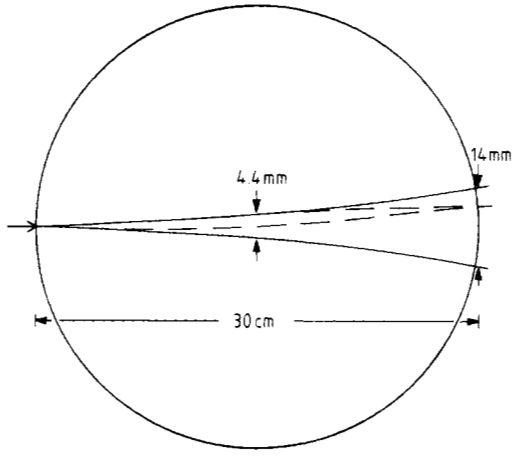

Figure 3. Predicted spreading of the FWHM of an initially collimated 230 MeV proton beam in 30 cm of water (solid line). Dashed line shows effect of restriction to a particular exit position.

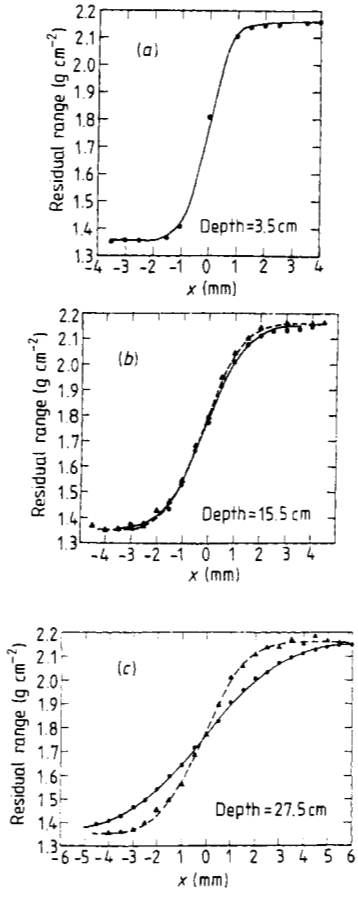

Figure 4. Edge response functions of 240 MeV proton beam at a depth of (*a*) 3.5 cm, (*b*) 15.5 cm, and (*c*) 27.5 cm in a 30.5 cm thick water bath. The dashed curves show the effect of a 2 mm wide restriction on the exit position.

The spatial resolution achieved in this experiment was measured by scanning 1 cm square Teflon pegs at various depths in a 30.5 cm thick water bath. The initial proton energy was 240 MeV. The edge response functions are shown in figure 4. The curves show the fit obtained using the integral of a Gaussian fitting function. At a depth of 3.5 cm the FWHM of the resolution function was 1.7 mm. Little effect is expected from a constraint on the exit position. At a depth of 15.5 cm the width was 3.0 mm FWHM for all events. Using only those protons that exited within a 2 mm wide band, the width was reduced to 2.7 mm, in good agreement with the convolution of the predicted 2.2 mm with the initial beam width of 1.7 mm. Near the rear of the water bath the resolution widths were 6.1 mm FWHM and 3.7 mm FWHM without and with exit constraint, respectively.

The unconstrained beam widths were not as wide as predicted because of the geometric restriction imposed by the trigger requirement that the protons pass through scintillator S2 and hit the HPGe detector. The width of the constrained events at a depth of 27.5 cm are wider than the 2 mm wide constraint because of the intervening 3.0 cm of water, 0.3 cm of aluminium, and 1.7 cm of air. When the CT scanning is done over an angle of 360° so that each ray is measured from opposite directions, the effective resolution near the edge of the water bath is predicted from these results to be about 2.6 mm FWHM and near the centre to be 2.7 mm FWHM.

The intrinsic limitations on the spatial resolution arising from multiple Coulomb scattering may be reduced through the use of heavy ions (Huesman *et al* 1975). Unfortunately, the use of alpha particles or even heavier ions reduces the dose advantage relative to protons.

6. Reconstructions

Two polyethylene phantoms were scanned. One phantom had a diameter of 19.3 cm. Forty-two million proton events were collected for this phantom at an incident energy of 192 MeV. A full 360° scan was taken with angular increments of 1.33°. The other phantom had a diameter of 29.5 cm. During a 45 h running period with an incident proton energy of 240 MeV, 62 million events were registered. A full scan was taken with angular step sizes of 1.0°.

The analysis of the data was carried out on a PDP-11/45. In this analysis, the events at each phantom position were sorted into eight groups according to their measured exit positions. Each group corresponded to a 2 mm wide cut in the exit position. The HPGe spectrum for each of the groups was fitted by the Gaussian weight method described in Appendix 1 to determine the mean energy and hence mean residual range of the protons in that group. The results were recorded on magnetic tape for subsequent reconstruction.

The reconstructions were performed on a CDC 7600 computer. Before reconstruction, the data obtained in each traverse scan were renormalised using both ends of the scan for which the proton beam passed only through the water bath. These end values were set to zero so that the processed projections measured deviations from the water value. Each exit position group, as explained above, was treated separately. A straight line approximation was made to the most probable path of the protons in each group. The angle of this line was taken to be that of the straight-through trajectory plus the exit displacement divided by the depth of the water bath. The exit position of the line was displaced from the straight-through trajectory by $\frac{5}{6}$ the exit displacement. The maximum deviation in this approximation was less than 1 mm. In effect, $8 \times 270 = 2160$

projections were used in the 19 cm diameter reconstruction and 2880 projections for 30 cm diameter reconstruction. The conventional filtered backprojection reconstruction algorithm was used (Shepp and Logan 1974). The projections were filtered in frequency space with a ramp function times a Gaussian where the Gaussian reached its half value at one half the reconstruction Nyquist frequency. Band-limited interpolation was used in the backprojection process. The reconstruction pixel sizes were 1.0×1.0 mm^2 for the 19 cm diameter and 1.25×1.25 mm^2 for the 30 cm diameter.

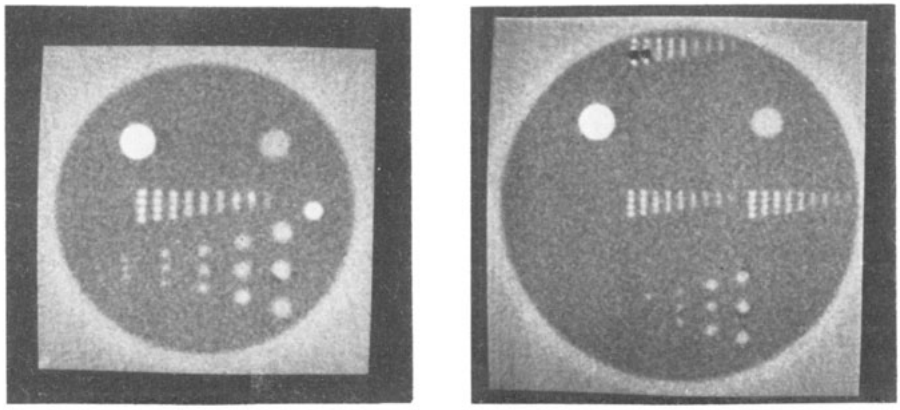

(*a*) (*b*)

Figure 5. Proton CT reconstructions for (*a*) 19.3 cm and (*b*) 29.5 cm diameter phantoms obtained at an average dose of 0.6 cGy. The contrast of the density resolution pattern (bottom) is 1.8% with hole diameters of 12.7 mm, 9.5 mm, 6.4 mm, 4.8 mm, and 3.2 mm.

The proton CT reconstructions of the two polyethylene phantoms are shown in figure 5. The phantoms were specially made to allow direct comparison between proton and x-ray scans by using materials with elemental composition similar to the background material for the two resolution patterns. The central spatial resolution pattern consisted of polyurethane-filled holes. In each row the centre-to-centre hole spacing was twice the hole diameter. The hole diameters varied from 3 mm to 1 mm in 0.25 mm steps. The measured contrast relative to the polyethylene was 10.7%. The resolving power in the 19 cm diameter scan is 2.25 mm, and in the 30 cm diameter case, 2.5 mm.

The density resolution pattern at the bottom of the phantom was made by pressing high-density polyethylene dowels into holes drilled in the normal density polyethylene blank. The hole diameters in successive rows were 12.7, 9.5, 6.4, 4.8, and 3.2 mm. The contrast was measured to be $1.8 \pm 0.2\%$. While the presence of the smallest diameter holes can be detected in the 19 cm diameter phantom, only the 6.4 mm diameter holes are readily observed in the 30 cm diameter phantom. Actually, one of the 4.8 mm diameter holes is visible but the other two are not. A high-dose, x-ray scan of this phantom showed these other two holes possess considerably smaller contrast than the rest probably arising from variations in the density of the material used.

The large diameter holes at the top of the phantoms were filled with nylon on the left and water on the right. The reconstructed density of the polyethylene is -1.8% and of the nylon is 14.5%, in reasonable agreement with that expected on the basis of the relative stopping powers of the materials (Janni 1966).

The polyethylene phantoms were scanned on an EMI 5005 x-ray scanner for comparison. The scanner was operated in the normal (20 s) scan mode at 140 kV_p,

28 mA with scan diameters of 24 cm and 32 cm. The EMI reconstructions are shown in figure 6. The spatial resolutions of the EMI scans are obviously better than the proton scans with resolving power of about 1.5 mm. The contrast sensitivity is observed to be better than the proton scan for the 20 cm diameter phantom and worse for the 30 cm diameter phantom. The quantitative comparison between the EMI 5005 performance and that of the proton scans will be made in the next section. The reconstructed density of the polyethylene is −10.8%, and of the nylon 8.0%. The contrast of the polyurethane relative to the polyethylene is 10.0%, essentially the same as measured with the protons.

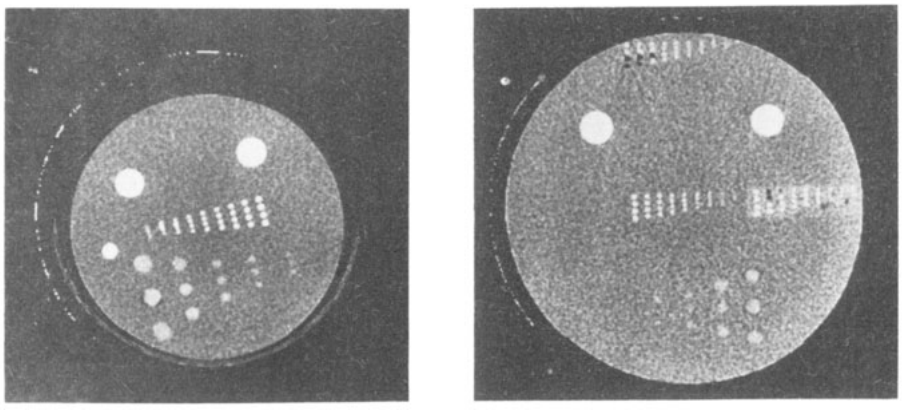

(*a*) (*b*)

Figure 6. EMI-5005 scans of (*a*) 19.3 cm and (*b*) 29.5 cm diameter phantoms. The average doses for these scans were 3.3 cGy and 2.2 cGy respectively.

7. Comparison with x-ray scanner

In this section we will compare the spatial resolution, contrast sensitivity and doses of the proton and x-ray scans obtained in this study. The spatial resolution was determined using the edge response of the nylon dowels in the phantoms. For the proton scans, Gaussian shape was assumed for the line response which is reasonable. Since the EMI response contained a 10% overshoot arising from the edge enhancement incorporated in the filter function (Hanson 1979b) this method could not be used. Instead, a smooth curve fit to the edge response was differentiated to obtain an approximate line response curve from which the FWHM was measured directly. The spatial resolutions are tabulated in table 1. The resolution for the 30 cm diameter

Table 1. Comparison of proton CT scans with those obtained with EMI CT-5005. NEQ provides a measure of contrast sensitivity as explained in text. The average dose is for a series of scans with 1 cm steps.

Method	Diameter (cm)	Spatial resolution (mm FWHM)	RMS noise (%)	NEQ (10^7 mm^{-1})	Average dose (cGy)	Proton dose advantage
Proton	19.3	3.4	0.24	4.2	0.44	4.5
EMI	19.3	1.6	0.63	7.1	3.3	
Proton	29.5	3.8	0.22	2.5	0.47	13
EMI	29.5	2.0	1.13	0.91	2.2	

phantom is approximately what is expected from the measured intrinsic resolution (section 4) when account is taken of the 2.2 mm FWHM blurring function associated with the reconstruction filter. The resolutions measured for the EMI scanner are somewhat worse than those obtained by Boyd *et al* (1976, 1977) presumably because of the limited number of edge scans used here.

Comparison of doses delivered by two different scanning techniques is incomplete without taking into account the relative contrast sensitivities. While the low contrast sections of the phantoms used in this experiment provide a rough measure of the contrast sensitivity, a more accurate procedure is desirable. The number of noise-equivalent quanta (NEQ) per unit length in the totality of projection measurements will be used here to provide a quantitative measure of contrast sensitivity. It has been shown (Hanson 1979b, Wagner *et al* 1979) that NEQ is directly related to the detection sensitivity index d' for the detection of large area, low contrast objects in an X-ray CT reconstruction. The NEQ may be determined either from a measurement of low frequency behaviour of the noise power spectrum or from the evaluation of the noise granularity function for large averaging areas (Hanson 1979b).

For the purpose of quoting an NEQ value for proton CT reconstructions, it was assumed that a change in the proton stopping power equivalent to water corresponds to a change in the linear attenuation coefficient in water of X-rays in the diagnostic energy region, that is 0.19 cm^{-1}. The NEQ values for the proton scans were determined from the measured RMS noise in the reconstructions and the relationship between the RMS noise and NEQ derived from the reconstruction filter function (equations (8) and (15) in Hanson (1979b)). These were checked by comparing the noise granularity computed from an 80×80 pixel section taken from a flat region in the reconstructions to that expected for the filter function used. Also, the NEQ agreed with the RMS noise in the projection measurements. The NEQ values for the EMI CT-5005 scans were found by scaling the NEQ measurements made on water phantoms such as those shown in Hanson (1979b) by the inverse mean square deviation of the noise in the reconstruction. These were also checked by a rough measurement of the noise granularity function. The NEQs given in table 1, accurate to about 5%, show the same relative ordering of the reconstructions in terms of contrast sensitivity as deduced qualitatively in the preceding section.

The doses given in table 1 are calculated as the average dose for a series of scans with 1 cm steps between scans. The proton doses are based on the number of incident protons required to obtain the number of protons detected in each scan neglecting any loss arising from deadtime in the electronics or scanner motion. Only the geometry of the apparatus is taken into account. For the 19 cm diameter scan, 34% of the incident particles resulted in triggers and for the 30 cm diameter scan, 28%. The loss of beam particles was approximately evenly accounted for by large angle deflection due to nuclear scattering in the water bath and phantom and by small angle multiple Coulomb scattering. The number of incident protons was reduced by a factor of $1.13^2 = 1.28$ to include the improvement in the range peak fitting procedure that could have been achieved through the use of an optimum weighting function as described in Appendix 1. The energy lost by the protons in traversing the water bath was calculated from the range–energy relation and it was assumed that nuclear-scattered protons, on the average, lose the same energy as the unscattered protons.

The doses for the EMI CT-5005 scans were derived from the measurements made by Boyd and his collaborators (Boyd *et al* 1977) on the same scanner used to obtain the reconstructions shown in figure 6. The dose for the 30 cm diameter phantom scan was

taken as the average dose measured on an elliptical phantom with a circumference of 91 cm. The dose for the scan of the 19 cm diameter phantom was scaled from measurements made on a 25 cm diameter water bath phantom assuming the average dose is inversely proportional to the phantom diameter, an assumption verified by Brosch *et al* (1978).

Table 1 summarises the relative dose efficiencies of the proton and X-ray scans given in terms of the ratio of NEQ to average dose. The proton dose advantage compared to the EMI CT-5005 is 3.5 for the 19 cm diameter phantom and 13 for the 30 cm diameter phantom. This means that at the same dose level, the contrast sensitivity could be improved by nearly a factor of two for 19 cm diameter phantoms and by over a factor of 3.5 for 30 cm diameter phantoms if the proton CT technique were employed instead of an EMI CT-5005 scanner. While the dose efficiency of the EMI scanner may be representative of present-day commercial X-ray scanners, it has been shown to be only about 12% compared to an ideal X-ray scanner that uses monoenergetic X-rays, perfect collimation and fully efficient detectors (Hanson 1979b). It may be feasible to construct practical X-ray scanners with three to four times higher dose utilisation. On the other hand, only about one half of the protons emerging from the back of the water bath were detected in the present equipment. With larger detectors the dose utilisation in the proton technique could be increased by almost a factor of two. In conclusion, the use of protons instead of X-rays could reduce the dose required to achieve a given contrast sensitivity for 30 cm diameter specimens by an order of magnitude. The advantage for 20 cm diameter specimens would be considerably less dramatic.

In the comparison between the use of protons and X-rays for diagnostic procedures, it will be desirable to compare the deleterious effects of the radiations upon humans. Unfortunately, there are no data on these effects in the dose range involved, namely, about 1 to 2 cGy. Measurements at doses of from 2 to 4 Gy indicate the RBE of 160 MeV protons are nearly the same as that of diagnostic X-rays (Hall *et al* 1978). While extrapolation to low doses by means of a model for cellular radiation damage indicates the RBE of protons may increase substantially, this procedure is highly speculative. Further, it is unclear whether single cell effects are at all related to the long-term response of complex organisms at these low doses.

8. Conclusion

We have demonstrated experimentally that reconstructions of diagnostic quality may be obtained using the proton energy-loss method. While the spatial resolution achievable by this method is fundamentally limited by multiple Coulomb scattering, it is not intolerable. The proton technique can achieve a given contrast sensitivity for a dose an order of magnitude lower than the X-ray transmission method for 30 cm diameter specimens. The proton dose advantage is significantly diminished for 20 cm diameter specimens. Since the proton method reconstructs the stopping power relative to some reference medium rather than the linear attenuation coefficient for X-rays, proton CT scans provide imaging characteristics different from X-ray scans. It is possible that this alternative imaging modality may provide diagnostic benefits when applied to clinical studies.

Acknowledgments

R Pehl and A Thomson of Lawrence Berkeley Laboratory constructed the HPGe detector used in this experiment. We gratefully acknowledge the assistance of

E Schneider, J Van Dyke, R Damjanovich, and O Rivera in setting up the apparatus. Many helpful discussions were held with M Goiten. P Berardo, S Zink and A Chavez provided help with the transferral of data from computer to computer. Thanks are due D Boyd and his collaborators for scanning our phantoms on the EMI CT-5005 and for providing unpublished dose measurements. The Gaussian weighted, iterative peak fitting procedure was suggested by K Klare. The consistent encouragement of L Rosen and E Knapp throughout this work is fully appreciated.

This work was supported by the US DOE, contract No W-7405-ENG-36.

Appendix 1. Peak fitting algorithms

We present here a method for determining the peak position of a distribution from a limited data sample. The method is based upon an iterative calculation of the weighted moment of the data and is generally useful. It is assumed that a histogram, such as an energy spectrum, is measured with n_i events in the ith bin where x_i specifies the position of that bin. First, it is assumed that only the position of the data relative to the x-axis is to be determined. Let the ensemble average of n_i be $f(x_i - a) = f_i$, where a is the peak position. The problem is to determine a from the data n_i. The procedure is to calculate the weighted moment which for the kth iteration is

$$\bar{x}_k = \frac{\sum x_i n_i w_i^k}{\sum n_i w_i^k} \tag{A1.1}$$

where the weighting function w_i^k is determined by the kth estimate of a, a_k:

$$w_i^k = w(x_i - a_k). \tag{A1.2}$$

The choice of weighting function will be discussed below. The next estimate for a is

$$a_{k+1} = \bar{x}_k + \Delta \tag{A1.3}$$

where Δ is the offset of the peak position from the weighted moment determined from the known function f as

$$\Delta = a - \sum x_i w_i f_i / \sum w_i f_i. \tag{A1.4}$$

Here Δ and w_i do not have a subscript since it is assumed that they are based on the known function f_i. More generally they might *depend* upon k. The initial choice for a_0 may be determined by (a) *a priori* information, (b) operator intervention or, (c) calculation of the moment of the data using a uniform weight function. In situations where the function f possesses only a single reasonably well-defined peak, the latter method works well.

The variance in the estimate of a obtained when this iterative method converges may be found by substitution of equation (A1.3) into equation (A1.1) setting $a_{k+1} = a_k$. Then differentiation of equation (A1.1) with respect to n_i yields

$$\sigma_a^2 = \sum \left(\frac{\partial a}{\partial n_i}\right)^2 \sigma_{n_i}^2 = \frac{\sum (x_i - \bar{x})^2 f_i w_i^2}{\left[\sum (x_i - \bar{x}) \dfrac{\partial f_i}{\partial x} w_i\right]^2} \tag{A1.5}$$

where the k subscript has been dropped, $\sigma_{n_i}^2 = n_i = f_i$ has been used and $\partial f_i / \partial x$ is the derivative of f evaluated at $x_i - a$.

In the analysis of the data obtained in this experiment, a Gaussian weight function was used and Δ was assumed to be zero:

$$w_i^k = \exp\left[-\frac{(w_i - a_k)^2}{2\sigma_k^2}\right]. \tag{A1.6}$$

The RMS width of the weighting function σ_k was varied in the iterative procedure to be the same as that of the fitting function, also assumed to be a Gaussian. Thus

$$\frac{1}{\sigma_{k+1}^2} + \frac{1}{\sigma_k^2} = \frac{\sum n_i w_i^k}{\sum (x_i - \bar{x}_{k-1})^2 n_i w_i^k}. \tag{A1.7}$$

An example of the results of this procedure when applied to the HPGe energy histogram data is shown in figure 1A. It is found that the iterative procedure converges rapidly and reliably with the Gaussian weighting function. This weighting function has the advantage that it removes the influence of long tails in the data, as seen in figure 1A, upon the peak position localisation. For example, the position of the energy peak in figure 1A is

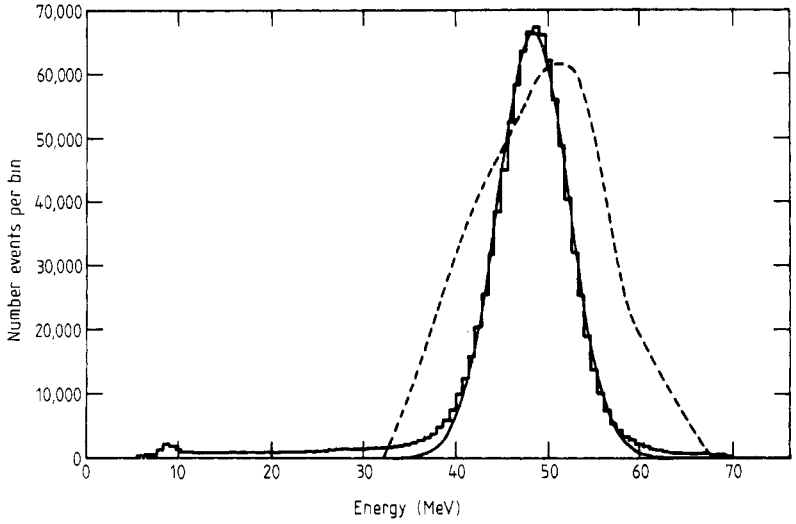

Figure 1A. The energy histogram obtained from the entire series of stability runs comprising 10^6 events. The curve shows the Gaussian fit to the data by the iterative fitting procedure described in the text.

determined by the uniformly weighted moment, 47.7 MeV. By equation (A1.5) the σ_a is the RMS width of the complete histogram, 8.13 MeV, divided by the square root of the number of events (a well known result). However, the uncertainty in a for the Gaussian weighted moment method given by equation (A1.5) 11 is 4.96 MeV divided by the square root of the number of events. The values of a and σ found by this method are 48.8 MeV and 3.85 MeV. Thus we see that the uniformly weighted moment results in a value for the peak position that is both biased as well as subject to a larger uncertainty than the Gaussian weighted moment by a factor of 1.64.

If the function f is known, it is feasible to determine the optimum weighting function. In general the maximum likelihood method yields the best estimate for unknown parameters. Under the assumption that the data values are normally distributed, valid when the number of events per bin is large, the maximum likelihood

condition may be restated as one of minimum chi-squared, where

$$\chi^2 = \sum \frac{(f_i - n_i)^2}{\sigma_{n_i}^2}. \tag{A1.8}$$

In fitting a single parameter, the peak position a, the minimum χ^2 is achieved when its derivative with respect to a is zero:

$$\frac{\partial \chi^2}{\partial a} = 2 \sum \frac{(f_i - n_i)}{\sigma_{n_i}^2} f_i' = 0 \tag{A1.9}$$

where f_i' is the derivative of f with respect to x evaluated at $x_i - a$. The variance in the estimate of a is given by

$$\frac{1}{\sigma_a^2} = \frac{1}{2} \frac{\partial^2 \chi^2}{\partial a^2} = \sum \frac{f_i'^2}{\sigma_{n_i}^2} = \sum \frac{f_i'^2}{f_i} \tag{A1.10}$$

where the variance in n_i has been replaced by $f_i = f(x_i - a)$, the ensemble average of n_i, appropriate for Poisson statistics. It is observed that the condition to be satisfied for minimum χ^2, equation (A1.9) is equivalent to the moment calculation, equations (A1.1, 3 and 4), at convergence ($a_{k+1} = a_k$) if the weighting function is chosen as

$$w_i^k = \frac{f_i'}{(x_i - a_k) f_i} \tag{A1.11}$$

and with $\sum w_i n_i$ inserted in the denominator in place of $\sum w_i f_i$ in equation (A1.4). Equation (A1.11) does not diverge at $x_i = a_k$ since it is assumed that a_k marks the peak position where $f_i' = 0$. Thus, the minimum χ^2 method provides the optimum weighting function for the iterative moment calculation. Equation (A1.5) yields equation (A1.10) under these conditions. Equation (A1.11) corresponds closely to a filter method for optimally finding peak locations developed by Gatti and Svelto (1966) and recently elaborated on by Llacer (1981).

Take as an example data that have a Gaussian shape in x. Then from equation (A1.11) it is found that the best estimate for the peak position is found using a uniform weighting function. This is the general result obtained by the maximum likelihood method. Furthermore, the uncertainty in a given by equation (A1.10) is the RMS width of the Gaussian divided by the square root of the number of events. If the Gaussian weighting procedure described by equations (A1.6 and 7) were used, then the uncertainty in the peak position, equation (A1.5) would be larger than this by a factor of $(8/3\sqrt{3})^{1/2} = 1.241$. Thus, while the Gaussian weight function may have some advantage in reducing the effects of events in the tails of the data distribution, it will not, in general, provide the best determination of the peak position.

The optimum weighting function to use in the moment calculation for the energy histogram in figure 1A has been estimated using equation (A1.11). It is shown as the dashed curve in figure 1A. The uncertainty in the peak position given by equation (A1.10) is 4.40 MeV divided by the square root of the number of events. This has been verified by breaking up the stability run into one-second samples, each containing an average of 861 events. The RMS peak position was found to be 0.156 ± 0.003 MeV, higher than the predicted value of 0.150 MeV by only 4%. When the same data were fitted using the Gaussian weighting function, the result was 0.178 ± 0.004 MeV, 4% higher than predicted. It is concluded that if the optimum weight method had been used to analyse the 19 cm diameter scan, the RMS noise in the reconstruction would have

been lower by a factor of 1.13. The similarity of the energy histogram obtained in the 30 cm diameter scan indicates a comparable reduction in noise is possible there, too.

Appendix 2. Alternative detectors

For the present experiment the hyperpure germanium detector was chosen to measure the residual proton range on account of its excellent stability. While the HPGe detector performed very well, it would be difficult to make it operate efficiently at event rates higher than about 50 kHz because of its slow rise time. As a consequence, two alternative range measurement schemes were investigated. Both are based on the use of plastic scintillators in conjunction with photomultiplier tubes. Since this arrangement can yield electronic pulses less than 10 ns long, instantaneous rates approaching 10 MHz may be accommodated without significant loss due to overlapping pulses.

In the first alternative detector, the protons were stopped in a block of scintillator. The pulse height of the photomultiplier viewing this scintillator should be roughly proportional to the proton energy. The scintillator, Nuclear Enterprises NE 102, was machined to a 4.9 cm long right circular cylinder with a diameter of 3.65 cm. The front of the scintillator was tapered over a distance of 1.9 cm to a front surface diameter of 2.9 cm. The scintillator was wrapped with aluminised Mylar to improve light collection. The back face of the scintillator block was glued directly to an EMI 9759 phototube. This photomultiplier was chosen for the inherent stability of its venetian blind dynode structure. The output pulse width was 30 ns FWHM. Our tube was selected by EMI for better than 0.5% gain stability over a 3 h period. The phototube and scintillator were contained in a Pacific Photometric Model 33 photomultiplier housing to stabilise the temperature since the gain change for an 11-stage photomultiplier is about 0.5% per °C (Liberman 1977, private communication). The temperature stability was measured to be about 0.4 °C over a 30 h period. The phototube base provided equal increments of voltage between all dynodes with double that increment between the first dynode and the photocathode.

The detector was calibrated in the same manner as described in section 4 at an operating voltage of 520 V. With $R_0 = 1.895$ g cm^{-2}, the exponent in equation (6) was found to be $\beta = 0.363$. The response of this detector showed some type of saturation effect since β is less than that observed for the HPGe. This is contrary to what is expected from the response of scintillators to low energy protons (Smith *et al* 1968), possibly because of the effect of the scintillator shape on light collection efficiency (Falk and Sparman 1970) or just photomultiplier saturation. When operated at 1000 V, the detector showed even worse saturation ($\beta = 0.23$). Table 1A summarises the stability results obtained for this detector from a series of 11 runs taken over a 13 min period for the 520 V operating voltage.

The second type of detector studied was a standard range telescope. It consisted of ten squares of NE 102 plastic scintillator each 0.246 ± 0.009 cm thick and wrapped in 0.005 cm thick shiny aluminium foil. Light from each scintillator was conducted to an EMI 9813B phototube through an adiabatic Plexiglas light pipe. Signals from the central eight counters were pulse height analysed by an LRS 2248. In addition, discriminators were used on all of the counter signals. The discriminator and pulse height information was recorded on magnetic tape by the on-line PDP-11.

The calibration of the range telescope was found to be 0.258 ± 0.002 g cm^{-2} per counter (β fixed at unity), slightly less than the 0.271 g cm^{-2} predicted from the counter thicknesses.

Table 1A. The RMS width of the range distributions and the RMS deviation of the mean range for a series of runs obtained with various detectors. The Gaussian weighted moment method was used throughout. The range telescope results are given for two energy thresholds. Here σ_R is the effective RMS range straggling.

Detector	Measurement	σ_R (g cm^{-2})	Events/run	RMS deviation of mean range	
				Predicted (mg cm^{-2})	Observed (mg cm^{-2})
HPGe	Energy deposited	0.285	25 800	2.30	2.42 ± 0.27
Scintillator	Energy deposited	0.318	27 500	2.51	2.29 ± 0.49
Range telescope	Range (1.2 MeV)	0.328	19 500	2.98	2.09 ± 0.52
	(7.1 MeV)	0.292	19 500	2.65	3.20 ± 0.80

For the stability series of runs, lasting 12 min, the proton stopping distribution was centred between counters 7 and 8. The energy calibrations of the pulse height spectra were determined from the energy lost by 192 MeV protons traversing the scintillator stack, roughly 10.6 MeV. The data were analysed by placing a threshold on the pulse height spectrum of each counter. A histogram of the last counter to exceed its threshold was used to represent the stopping distribution. Very few holes in the pattern of counters that fired were observed. The results of the eight stability runs are given in table 1A for two energy thresholds, assuming a linear energy scale. Since counter 10 registered all the particles that passed through it, not just those that stopped in it, counter 10 presented an anomalously high response.

Note that as the threshold energy is increased, so is the depth into the counter that a proton must penetrate to produce that energy. This depth we call the counter's dead layer. Taking into account the nonlinear response of the scintillator to low-energy protons (Smith *et al* 1968), the actual proton energies corresponding to the thresholds given in table 1A are estimated to be 3.7 MeV and 13.0 MeV. The corresponding water equivalent dead layers are 20 mg cm^{-2} and 193 mg cm^{-2} (Janni 1966). The shift in the stopping distribution between these thresholds was 0.38 counter widths or 98 mg cm^{-2}. The dead layer is important since instabilities in photomultiplier gain produce changes in the stopping distribution relative to the dead layer. The thinner the dead layer, the smaller the effect of photomultiplier gain instabilities. Thus, quite poor stabilities in the photomultiplier gains may be tolerated in a range telescope if the dead layer is small enough. This effect is perhaps responsible for the improved stability observed for the lower threshold. However, the anomalous behavior of counter 10 may be the cause of this as well as of the larger range straggling for the 1.2 MeV threshold.

Comparison of the three detectors studied in the course of this experiment shows the range straggling to be similar, with the HPGe straggling the smallest. The expected range straggling of a 192 MeV proton beam in water is 0.284 g cm^{-2} in good agreement with the HPGe measurement. The width of the range telescope distribution is expected to be about 3% larger or 0.294 g cm^{-2} because of the finite widths of the range bins. The predicted RMS deviation of the mean range was estimated as 1.24 times the effective RMS range straggling divided by the square root of the number of events in the Gaussian fitted peaks (Appendix 1). We observe that none of the detectors showed an RMS deviation that was larger than one standard deviation above that predicted. We conclude that all of these range detection methods possess an RMS stability of better than a few mg cm^{-2}, sufficient for use in proton computed tomography.

Résumé

Tomographie computérisée utilisant la perte d'énergie des protons.

Nous avons fait une expérimentation afin de montrer la possibilité d'éffectuer de la tomographie computérisée par protons. Nous avons utilisé la perte d'énergie des protons pur mesurer les projections des pouvoirs d'arrêt relatifs des fantômes. Nous avons obtenu des reconstructions de haute qualité à partir des images de fantômes de 19 cm et 30 cm de diamètre. La comparaison avec les reconstructions obtenues à partir d'un tomodensitomètre à rayons X EMI CT 5005 montre que la technique utilisant des protons est beaucoup plus éfficace pour une dose reçue par le malade.

Zusammenfassung

Computertomographie mit Hilfe des Protonenenergieverlustes.

Vorgestellt wird ein Experiment, daß die Eignung der Protonencomputertomographie demonstriert. Man benutzte den Protonenenergieverlust zur Messung der Projektionen des relativen Bremsvermögens der Phantome. Aus Scans von Phantomen mit 19 und 30 cm Durchmesser erhielt man qualitativ hochwertige Rekonstruktionen. Der Vergleich mit Rekonstruktionen von einem EMI CT 5005 Röntgenstrahlscanner zeigt, daß die Protonentechnik im Hinblick auf die niedrigere Strahlenbelastung bei vergleichbarer Bildgüte viel effizienter ist.

References

Benton E V, Henke R P, Tobias C A and Cruty M R 1975 *Radiography with Heavy Particles at Donner Laboratory* LBL-2887

Berger J, Duchazeaubeneix J C, Faivre J C, Garretta D, Legrand D, Rouger M, Saudinos J, Rayboud C and Salamon G 1978 *J. Comput. Assist. Tomogr.* **2** 488

Boyd D P, Korobkin M M and Moss A A 1976 *SPIE* **96** 303

Boyd D P, Margulis A R and Korobkin M M 1977 *SPIE* **127** 280

Brosch R C, Boyd D P and Gooding C A 1978 *Am. J. Roentgenol.* **131** 95

Capp M P, Sommer F G, Tobias C A and Benton E V 1978 *SPIE* **152** 72

Cookson J A 1974 *Naturwiss.* **61** 184

Cormack A M 1963 *J. Appl. Phys.* **34** 2722

Cormack A M 1964 *J. Appl. Phys.* **35** 2908

Cormack A M and Koehler A M 1976 *Phys. Med. Biol.* **21** 560

Crowe K M, Budinger T F, Cahoon J L, Elischer V P, Huesman R H and Kanstein L L 1975 *IEEE Trans. Nucl. Sci.* **NS-22** 1752

Duchazeaubeneix J C, Faivre J C, Garretta D, Guillerminet B, Rouger M, Saudinos J, Palmieri P, Raybaud C, Salamon G, Charpak G, Melchart G, Perrin Y, Santiard J C and Sauli F 1980 *J. Comput. Assist. Tomogr.* in press

Falk F and Sparman P 1970 *Nucl. Instrum. Meth.* **85** 253

Gatti E and Svelto V 1966 *Nucl. Instrum. Meth.* **39** 309

Goitein M 1972 *Nucl. Instrum. Meth.* **101** 509

Hall E J, Kellerer A M, Rossi H H and Lam Y P 1978 *Int. J. Radiat. Oncol. Biol. Phys.* **4** 1009

Hanson K M 1978, *Development of a Proton Radiographic System for Diagnosis and Localisation of Soft-Tissue Abnormalities* LA-7107-MS

Hanson K M, Bradbury J N, Cannon T M, Hutson R L, Laubacher D B, Macek R, Paciotti M A and Taylor C A 1978 *IEEE Trans. Nucl. Sci.* **NS-25** 657

Hanson K M 1979a in *Proc. Computer Aided Tomography and Ultrasonics in Medicine, Haifa, Israel* (Amsterdam: IFIP/North-Holland); reprinted in *IEEE Trans. Nucl. Sci.* **NS-26** 1635

Hanson K M 1979b *Med. Phys.* **6** 441

Huesman R H, Rosenfeld A H and Solnitz F T 1975 *Comparison of Heavy Charged Particles and X Rays for Axial Tomographic Scanning* LBL-3040

Janni J F 1966 *U.S. Air Force Weapons Laboratory Technical Report* No AFWL-TR 65-150

Koehler A M 1968 *Science* **160** 303

Kramer S L, Moffett D R, Martin R L and Colton E P 1979 *Proton Radiography* to be published

Llacer J 1981 *IEEE Trans. Nucl. Sci.* **NS-28** 630

Moffett D R, Colton E P, Concaildi G A, Hoffman E W, Klem R D, Knott M J, Kramer S L, Martin R L, Parker E F, Passi A R, Schultz P F, Stockley R L, Timm R E, Skaggs L S and Steward V W 1975 *IEEE Trans. Nucl. Sci.* **NS-22** 1749

Shepp L A and Logan B F 1974, *IEEE Trans. Nucl. Sci.* **NS-21** 21

Smith D L, Polk R G and Miller T G 1968 *Nucl. Instrum. Meth.* **64** 157

Steward V W and Koehler 1973a *Science* **179** 913

Steward V W and Koehler A M 1973b *Nature* **245** 38

Steward V W and Koehler A M 1974 *Radiology* **110** 217

Wagner R F, Brown D G and Pastel M S 1979 *Med. Phys.* **6** 83